Journal of Energy Chemistry 47 (2020) 18–28

Contents lists available at ScienceDirect

Journal of Energy Chemistry

journal homepage: www.elsevier.com/locate/jechem

http://www.journals.elsevier.com/journal-of-energy-chemistry/

Research article

An investigation of Zr/Ce ratio influencing the catalytic performance of $CuO/Ce_{1-x}Zr_xO_2$ catalyst for CO_2 hydrogenation to CH_3OH

Weiwei Wang[a,b], Zhenping Qu[a,*], Lixin Song[a], Qiang Fu[b,*]

[a] Key Laboratory of Industrial Ecology and Environmental Engineering, School of Environmental Science and Technology, Dalian University of Technology, Dalian 116024, Liaoning, China

[b] State Key Lab of Catalysis, Dalian Institute of Chemical Physics, Chinese Academy Sciences, Dalian 116023, Liaoning, China

ARTICLE INFO

Article history:
Received 27 September 2019
Revised 19 November 2019
Accepted 24 November 2019
Available online 29 November 2019

Keywords:
CO_2 hydrogenation
$Ce_{1-x}Zr_xO_2$
m-HCOO*
bi-HCOO*
in-situ DRIFTS

ABSTRACT

A series of $CuO/Ce_{1-x}Zr_xO_2$ catalysts (x = 0.2, 0.4, 0.6 and 0.8) are applied to elaborate the effect of the Zr/Ce ratio on the catalytic performance of CO_2 hydrogenation to CH_3OH. The best catalytic performance is achieved with $CuO/Ce_{0.4}Zr_{0.6}O_2$, exhibiting X_{CO2} = 13.2% and Y_{CH3OH} = 9.47% (T = 280 °C, P = 3 MPa). The formation of dispersed surface CuO species and larger number of oxygen vacancies are detected over $CuO/Ce_{0.4}Zr_{0.6}O_2$ due to stronger interaction between CuO and $Ce_{0.4}Zr_{0.6}O_2$, resulting in the superior activation ability for H_2 and CO_2 respectively. Additionally, the evidence is provided by *in situ* DRIFTS under the activity test pressure (3 MPa) that bi/m-HCOO* species are preferable for accumulating over ceria-rich ($CuO/Ce_{0.6}Zr_{0.4}O_2$ and $CuO/Ce_{0.8}Zr_{0.2}O_2$) catalysts while zirconia-rich ($CuO/Ce_{0.4}Zr_{0.6}O_2$ and $CuO/Ce_{0.2}Zr_{0.8}O_2$) catalysts are benefit to encourage the transformation of bi/m-HCOO* species to CH_3OH. The abundant population and high activity of intermediate species over $CuO/Ce_{0.4}Zr_{0.6}O_2$ give a strong positive effect on the catalytic performance.

1. Introduction

CO_2 reuse is a mandatory key step to achieve a sustainable and carbon-neutral anthropogenic cycle. CH_3OH is an excellent liquid fuel and a feedstock for the manufacture of chemicals that is also reasonably safe to use and transport [1]. The applicability of copper-based catalysts in the synthesis of CH_3OH via CO_2 hydrogenation is broad because of the ample evidence that copper commonly dispersed on metal oxide substrate due to the metal-support interaction effect [2,3]. Many studies are dedicated to improve its efficiency by introducing various oxides, such as zirconia [4], ceria [5], alumina-doped ceria [6], gallium [7], and lanthana [8]. In addition, Cu/CeO_2 is regarded in general as more active catalytic system than others for CO_2 hydrogenation, because the interaction effect between Cu and CeO_2 is responsible for the enhanced activity of CO_2 hydrogenation [9,10]. Nevertheless, it still shows the unsatisfactory CH_3OH selectivity at decent CO_2 conversion over copper-based catalysts. It has been reported that the addition of ZrO_2 to CeO_2 leads to improvements in oxygen storage capacity of CeO_2, redox property and promotion of metal dispersion due to the partial substitution of Ce^{4+} with Zr^{4+} in the lattice of CeO_2 resulting in solid solution formation [11]. $Ce_{1-x}Zr_xO_2$ solid solution is found indeed to improve metal-support interaction with beneficial effect on catalytic performance, and has a huge number of applications, such as a direct component or a support, ranging from CO oxidation [12], selective catalytic reduction NO by NH_3 [13], automotive emission control [14] to water-gas shift reaction [15]. However, its application in CO_2 hydrogenation is very limited. In fact, $Ce_{1-x}Zr_xO_2$ solid solution has higher basicity or electron-donating ability and can assist the conversion of CO_2 [16]. Additionally, oxygen vacancies are also more easily generated in the $Ce_{1-x}Zr_xO_2$ solid solution, which are profitable in hydrogenation reactions [17]. Therefore, $Ce_{1-x}Zr_xO_2$ solid solution supported copper catalyst is expected to have a beneficial effect on the CO_2 hydrogenation to CH_3OH activity. Moreover, the extent of promotion effect of $Ce_{1-x}Zr_xO_2$, giving rise to different degrees of interaction between Cu and $Ce_{1-x}Zr_xO_2$ solid solution, is known to depend on the variable Zr/Ce ratios for selective catalytic reduction of NO with NH_3, reforming of ethylene glycol [18–20].

The present work is focused on the effect of incorporating Zr^{4+} into CeO_2 on the catalytic performance of $CuO/Ce_{1-x}Zr_xO_2$ for hydrogenation of CO_2 to CH_3OH. *In situ* Diffuse Reflectance Infrared Fourier Transform spectroscopy (*in situ* DRIFTS) is conducted to

* Corresponding authors.
E-mail addresses: quzhenping@dlut.edu.cn (Z. Qu), qfu@dicp.ac.cn (Q. Fu).

https://doi.org/10.1016/j.jechem.2019.11.021

get insight into the reactivity of the intermediate species for CO_2 hydrogenation to CH_3OH, elucidating the underlying mechanism of the experimentally observed synergistic effect on promoting CH_3OH formation over $CuO/Ce_{1-x}Zr_xO_2$ catalysts.

2. Experimental

2.1. Preparation of catalysts

$CuO/Ce_{1-x}Zr_xO_2$ (x = 0.2, 0.4, 0.6, 0.8) catalysts were prepared by an oxalate coprecipitation method using copper (II), cerium (IV) nitrate and zirconium (IV) nitrate as precursors. The desired amounts of precursors were dissolved separately in distilled water under 70 °C stirring conditions and mixed together for 1 h. Then the samples were aged for 2 h at room temperature. The obtained samples were dried at 80 °C overnight and subsequently calcined at 450 °C for 4 h at a heating rate of 5 °C/min in air atmosphere to obtain the final oxide materials. Then the materials were crushed and sieved to a size range of 40–60 mesh. The final $CuO/Ce_{0.8}Zr_{0.2}O_2$, $CuO/Ce_{0.6}Zr_{0.4}O_2$, $CuO/Ce_{0.4}Zr_{0.6}O_2$ and $CuO/Ce_{0.2}Zr_{0.8}O_2$ catalysts was labeled as x = 0.2, x = 0.4, x = 0.6 and x = 0.8, respectively. The traditional $CuO/ZnO/Al_2O_3$ catalysts were prepared by Na_2CO_3 co-precipitation method [21].

2.2. Catalyst characterization

XRD patterns were collected on a using XRD (D/max 22000) instrument equipped with nickel-filtered Cu $K\alpha$ (0.15418 nm) radiation source and a scintillation counter detector. The Raman spectra were obtained at room temperature using a LabRam HR800. The BET surface areas were determined by N_2 physisorption at liquid N_2 temperature on a Quanta chrome Autosorb SI instrument. XPS analysis was carried out on ESCALAB250 with an Al $K\alpha$ spectrometer. All binding energies were measured within a precision of ±0.3 eV. The metallic copper surface area (S_{cu}) and dispersion (D_{cu}), particle size (d_{cu}) was determined by using N_2O chemisorption according to the procedure described by Van Der Grift et al. [22].

The temperature-programmed reduction of H_2 (H_2-TPR) was conducted on a Chembet PULSAR TPR/TPD instrument. 50 mg of the sample was used in each measurement. The samples were first pre-treated under He (120 mL/min) at 200 °C for 0.5 h, and then cooling down to room temperature. After that, the gas flow was switched to 10 vol% H_2/He, and the sample was heated to 500/900 °C at a rate of 10 °C/min.

The temperature-programmed desorption of H_2 (H_2-TPD) was studied using the same apparatus as for H_2-TPR. Firstly, 100 mg of the pre-reduced sample (ν = 50 mL/min, pure H_2, 300 °C, 3 h) was degassed for 0.5 h in flowing He at 300 °C followed by cooling down to 30 °C. Then the sample was saturated with a mixture of H_2/He, followed by purging with He for 1 h to remove the physically adsorbed H_2. After that the sample was heated from 30 to 750 °C in He at a ramp of 10 °C /min.

The temperature-programmed desorption of CO_2 (CO_2-TPD) was performed on a quadrupole mass spectrometer (QMS, Pfeiffer OmniStar). The catalyst was firstly reduced, and then pre-treated in He at 310 °C for 0.5 h. Next, the samples were saturated with CO_2/He at around 30 °C for 30 min and then flushed with He to evacuate the surface physisorbed CO_2. TPD experiment was operated from 30 to 450 °C for CO_2-TPD.

In situ diffuse reflectance infrared Fourier transform spectroscopy (*in situ* DRIFTS) analysis was applied to evaluate the evolution of the intermediate species under $V(CO_2)$:$V(H_2)$ = 1:3 atmosphere at 280 °C and 3 MPa. Spectra were recorded with Vertex 70, Bruker equipped with a liquid N_2 cooled MCT detector. The pre-reduced sample was firstly exposed to pure N_2 at the same total flow rate (60 mL/min) as the reaction. After sweeping, the system was added into the mixture gas CO_2 + N_2 until reaching adsorption saturation, and then the gas H_2 + CO_2 substituted for CO_2 + N_2. The spectra of intermediate species were recorded as a function of time at 280 °C. The scans were collected ranging from 4000 to 800 cm^{-1} at a resolution of 4 cm^{-1}. The intensities were evaluated in Kubelka–Munk units, which were linearly related to the coverage of adsorbed species on the catalyst surface.

2.3. Catalytic activity measurement

The evaluation of catalyst activity was conducted using a fixed bed continuous-flow reactor packed with 0.5 g of H_2-reduced catalyst. The temperature of the catalyst bed was tested as reaction temperature by inserting a thermal couple into the catalyst. Then, the gas mixture containing $V(CO_2)/V(H_2)$ = 1/3 was fed into the reactor with a space velocity of 10,000 h^{-1}. Meanwhile, the temperature increased from 200 to 300 °C with a heating rate of 5 °C/min and kept at each temperature (200, 220, 240, 260, 280 and 300 °C) for 2 h. The reaction gas (CO_2) and reaction by-product (CO) were analyzed with GC7890T equipped with thermal conductivity detector (TCD) and Porapak-Q column, and the products (including CH_3OH and CH_4) was analyzed by using GC7900 equipped with a flame ionization detector (FID) and a capillary column. The carbon balance in the reaction reaches above 98%.

$$X_{CO2}(\%) = \frac{[CO_2]_{in} - [CO_2]_{out}}{[CO_2]_{in}} \times 100$$

$$S_{CH_3CH}\ (\%) = \frac{[CO_3OH]_{out}}{[CO_2]_{in} - [CO_2]_{out}} \times 100$$

$$Y_{CH_3OH}(\%) = X_{CO_2}(\%) \times S_{CH_3OH} \times 100$$

$$\mathrm{TOF} = \frac{\mu_{CO_2} X_{CO_2} M_{Cu}}{V_m w_{Cu} m_{cat} D_{Cu}}$$

$[CO_2]_{in}$ and $[CO_2]_{out}$ are CO_2 inlet and outlet amounts (mmol/min), respectively.

$[CH_3OH]_{out}$ is CH_3OH amount (mmol/min) in the product.

μ_{CO2} is CO_2 flow rate in the feed gas, X_{CO2} is CO_2 conversion, M_{Cu} is molar mass of Cu; V_m is standard molar volume of gas; w_{Cu} is mass percent of Cu (28%), m_{cat} is catalyst mass; D_{Cu} is the dispersion of Cu which is calculated through the N_2O chemisorption.

3. Results and discussion

3.1. Structural and textural properties

The textual properties of $CuO/Ce_{1-x}Zr_xO_2$ catalysts are given in Table 1. And it is found that the surface area (S_{BET}), pore volume (PV) and pore diameter (PD) rises with the increase of Zr/Ce ratio from x = 0.2 to x = 0.6, and then drops with the further increase of Zr/Ce ratio. The $CuO/Ce_{0.4}Zr_{0.6}O_2$ sample possesses the largest surface area (117.6 m^2/g). The same changing trend occurs for PV and PD. The representative SEM images of four samples are shown in Fig. 1. All samples exhibit a nano-crystal nature with irregular morphology and the Zr/Ce ratio shows significant influence on the grain size. Nanoparticles with 10–15 nm in size are predominant for the x = 0.6 sample, which is smaller than those of x = 0.2, 0.4 and 0.8 in general. Moreover, the morphology of $CuO/Ce_{0.4}Zr_{0.6}O_2$ is more uniform than others.

XRD patterns of $Ce_{1-x}Zr_xO_2$ and $CuO/Ce_{1-x}Zr_xO_2$ materials are presented in Fig. 2. As can be noted from Fig. 2(a), with regard to all the samples, no characteristic diffraction peaks of ZrO_2 are observed. The diffraction peaks of CeO_2 for $Ce_{1-x}Zr_xO_2$ shift to higher values of 2θ compared with pure CeO_2 with the increase

Table 1. Textural and structural properties of $Ce_{1-x}Zr_xO_2$ and $CuO/Ce_{1-x}Zr_xO_2$ catalysts.

Catalyst	$Ce_{1-x}Zr_xO_2$ cell parameter	$CuO/Ce_{1-x}Zr_xO_2$ cell parameter	d_{CuO}[a] (nm)	S_{BET} (m^2/g)	PV[b] (cm^3/g)	PD[b] (nm)	S_{cu}[c] (m^2/g)	D_{cu}[c] (%)	d_{cu}[c] (nm)
CeO_2	5.441	5.441	NA	NA	NA	NA	NA	NA	NA
$x = 0.2$	5.418	5.411	25.4	38.9	0.15	3.4	29.4	4.9	20.2
$x = 0.4$	5.426	5.372	20.7	41.8	0.11	3.7	40.9	5.2	19.1
$x = 0.6$	**5.248**	**5.158**	**13.6**	**117.6**	**0.29**	**8.1**	**64.7**	**9.5**	**10.5**
$x = 0.8$	5.283	5.197	15.1	54.1	0.19	3.8	49.5	5.4	18.4

S_{BET} data from BJH pore size distribution desorption branch.
The catalyst ***x* = 0.6** shows the best catalytic performance, hence, its corresponding values are bold.
[a] Determined by XRD data.
[b] Pore Volume (PV) and Pore Diameter (PD) data from BJH pore size distribution desorption branch.
[c] Determined by N_2O chemisorption method.

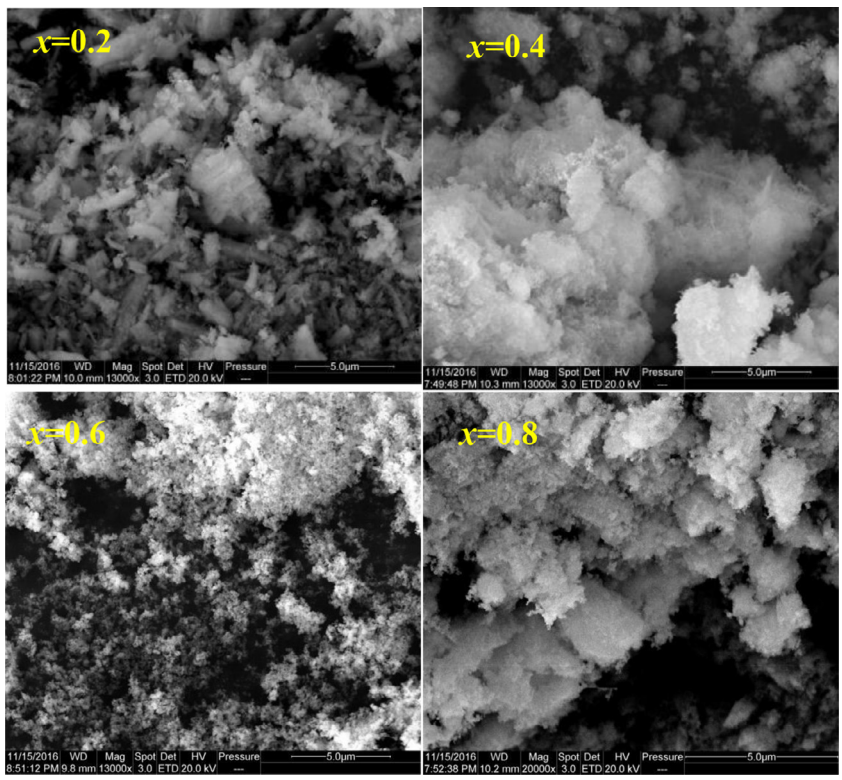

Fig. 1. SEM images of $CuO/Ce_{1-x}Zr_xO_2$ catalysts.

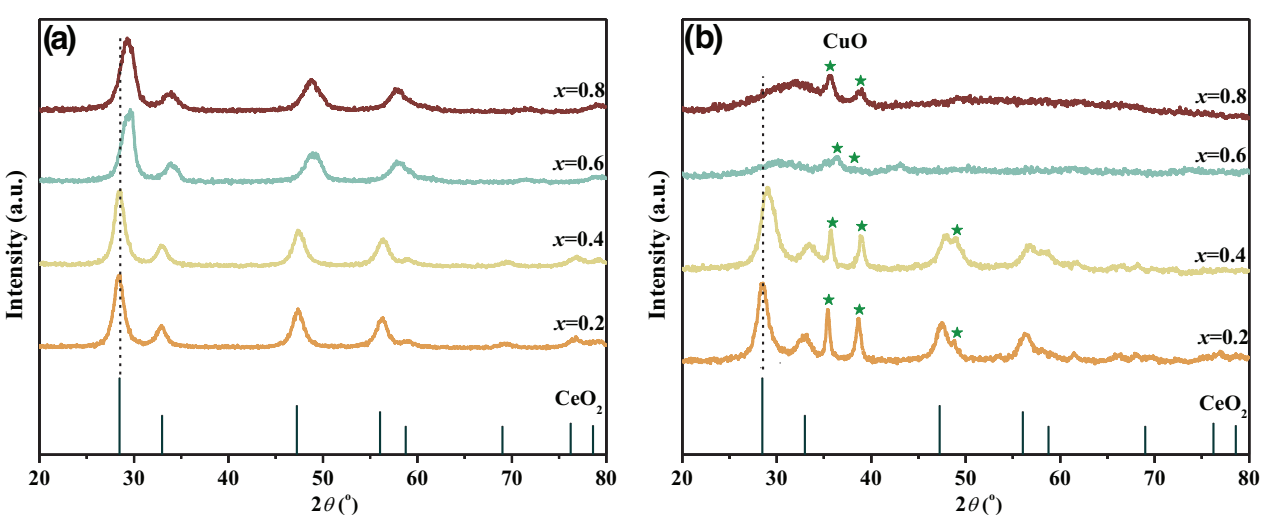

Fig. 2. XRD patterns of $Ce_{1-x}Zr_xO_2$ (a) and $CuO/Ce_{1-x}Zr_xO_2$ (b) catalysts.

Table 2. H_2-TPR and XPS data measured for $CuO/Ce_{1-x}Zr_xO_2$ catalysts.

Catalyst	$\alpha/(\alpha+\beta+\gamma)$	$\beta/(\alpha+\beta+\gamma)$	$Ce^{3+}/(Ce^{3+}+Ce^{4+})$ (%)	$(O_\beta+O_\gamma)/(O_\alpha+O_\beta+O_\gamma)$ (%)	$Cu^0/(Cu^0+Cu^{2+})$ (%)
$x = 0.2$	18.1	50.5	15.1	35.7	70.2
$x = 0.4$	23.7	56.9	18.6	49.1	76.1
$x = 0.6$	**31.4**	**64.4**	**29.4**	**76.2**	**88.6**
$x = 0.8$	28.8	57.4	25.4	57.2	82.4

The catalyst ***x* = 0.6** shows the best catalytic performance, hence, its corresponding values are bold.

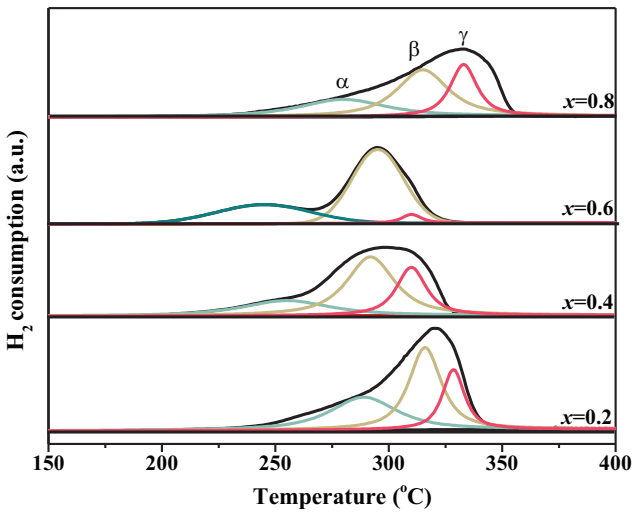

Fig. 3. H_2-TPR profiles of $CuO/Ce_{1-x}Zr_xO_2$ catalysts.

of Zr/Ce ratio, which is consistent with a decrease in the lattice cell parameter on the substitution of Ce^{4+} by Zr^{4+} cations (Table 1), forming $Ce_{1-x}Zr_xO_2$ solid solution [23]. When Zr/Ce ratio is further increased to $x = 0.8$, the peak position shifts back to lower angle along with the increase in lattice cell parameter (Table 1), which demonstrates the decrease of the amount of substitution of Zr^{4+} into CeO_2 unit cell. After copper is added on $Ce_{1-x}Zr_xO_2$ (Fig. 2b), the positions of the diffraction peaks of $Ce_{1-x}Zr_xO_2$ solid solution are further shifted to higher 2θ value. The lattice cell parameters of $CuO/Ce_{1-x}Zr_xO_2$ are lower than those of $Ce_{1-x}Zr_xO_2$ supports, which can be attributed to the introduction of Cu^{2+} into $Ce_{1-x}Zr_xO_2$ support [24]. Additionally, it can be seen that the peaks associated with CuO species are observed over $CuO/Ce_{1-x}Zr_xO_2$ catalysts. The width and intensity of CuO peaks vary with the Zr/Ce ratio due to the different strength interaction effect between CuO and $Ce_{1-x}Zr_xO_2$ solid solution [25]. The crystallite size of CuO (2θ=35.3°) determined by Scherrer equation decreases from 25.4 nm ($x = 0.2$) to 20.7 nm ($x = 0.4$), 13.6 nm ($x = 0.6$) and then increases to 15.1 nm ($x = 0.8$), showing that $x = 0.6$ is provided with stronger interaction between CuO and $Ce_{0.4}Zr_{0.6}O_2$ solid solution. Above all, it is demonstrated that there are two types of CuO species, namely surface CuO species and Cu^{2+} in the Cu–Ce–Zr solid solution, on all samples. What's more, $CuO/Ce_{0.4}Zr_{0.6}O_2$ displays the best fine dispersion of surface CuO and forms the largest number of Cu–Ce–Zr solid solution.

3.2. Effect of Zr/Ce ratio on the reducibility of catalysts

The H_2-reduction profiles of $CuO/Ce_{1-x}Zr_xO_2$ catalysts are shown in Fig. 3. For all CuO-based catalysts, reduction peaks of CuO are centered in the range of 230–350 °C and deconvoluted into three peaks. The α peak at lower temperature (240–260 °C) is assigned to the reduction of Cu^{2+} in the Cu–Ce–Zr solid solution [26]. The β peak (290–305 °C) corresponds to the reduction of small crystalline sized CuO species. The γ peak (310–330 °C) is the reduction of CuO species with large crystalline particle size. Both α and β peak areas of $CuO/Ce_{0.4}Zr_{0.6}O_2$ catalyst are the highest among theses $CuO/Ce_{1-x}Zr_xO_2$ catalysts, indicating the presence of a larger number of Cu–Ce–Zr solid solution and more dispersed CuO with small size compared with other samples (Table 2). This result is consistent with XRD results. Meanwhile, the reduction peaks in $x = 0.6$ sample appear at lower temperatures compared with those in other samples, which means that a stronger interaction does exist between copper species and $Ce_{0.4}Zr_{0.6}O_2$ solid solution in the $CuO/Ce_{0.4}Zr_{0.6}O_2$ catalysts, and Cu^{2+} species can be easily reduced. XPS results (Fig. 4a and Table 2) show that Cu^0 species (>70%) are the dominant ones over these $CuO/Ce_{1-x}Zr_xO_2$ catalysts after H_2 reduction, and $CuO/Ce_{0.4}Zr_{0.6}O_2$ catalyst has higher concentration of Cu^0 species (88.6%) than others due to the better reducibility of the catalyst.

To verify the properties of the Cu^0 species of the H_2-reduced $CuO/Ce_{1-x}Zr_xO_2$ catalysts, Cu dispersion (D_{cu}) and Cu surface area (S_{cu}) determined by N_2O chemisorption are listed in Table 1. It can be seen that D_{cu} increases with the increasing of Zr/Ce ratio from $x = 0.2$ to $x = 0.6$ and then decreases when $x = 0.8$. The $x = 0.6$ sample shows a significantly high Cu dispersion of 9.5%, and similarly, the S_{Cu} of $x = 0.6$ gives 64.7 m^2/g, which is larger than that of other samples.

3.3. Effect of Zr/Ce ratio on the formation of oxygen vacancies

The Raman spectroscopy is sensitive to both M–O bond arrangement and oxygen vacancies. The differences within the oxygen displacement of the $Ce_{1-x}Zr_xO_2$ solid solution are investigated by Raman spectroscopy. As is shown in Fig. 5(a), there exists a peak at 290 cm^{-1} associated with CuO species Raman band for $CuO/Ce_{1-x}Zr_xO_2$ samples. Pure CeO_2 shows a single strong Raman band at 463 cm^{-1}, which is ascribed to the vibration mode of the fluorite structure [24]. It is found that the peak at 463 cm^{-1} becomes weak and broad for all $CuO/Ce_{1-x}Zr_xO_2$ compared with CeO_2, more importantly, this kind of broadness is the most obvious for $CuO/Ce_{0.4}Zr_{0.6}O_2$ samples, demonstrating that the larger amounts of Cu–Ce–Zr solid solution form over $x = 0.6$ sample. Two bands at approximate 310 cm^{-1} and 632 cm^{-1} assigned to the displacement of oxygen atoms from their ideal fluorite lattice positions and nondegenerate Longitudinal Optical (LO) mode of ceria respectively appear, which is resulted from the substitution of Ce^{4+} with Zr^{4++} [27]. The ratio of the two peaks at 632 cm^{-1} (denoted as A_{632}) and at 463 cm^{-1} (denoted as A_{463}) can represent the relative oxygen vacancy sites [28]. The peak fitting for 632 cm^{-1} and 463 cm^{-1} is plotted in Fig. 5(a). The higher A_{632}/A_{463} value of 1.51 for $x = 0.6$ (Fig. 5b) suggests the presence of larger number of oxygen vacancy sites, compared with the values of 0.41, 0.62, and 0.71 for $x = 0.2$, $x = 0.4$ and $x = 0.8$, respectively. The changing trend surface relative $Ce^{3+}/(Ce^{4+}+Ce^{3+})$ is same to the variation of oxygen vacancies concentration (Table 2 and Fig. 4b). The concentration of $Ce^{3+}/(Ce^{4+}+Ce^{3+})$ is in order: $x = 0.6$ (29.4%) > $x = 0.8$ (25.4%) > $x = 0.4$ (18.6%) > $x = 0.2$ (15.1%). The transformation of Ce^{4+} to Ce^{3+} can create the charge imbalance and oxygen vacancy on the catalyst according to the charge compensation. Meanwhile the relative amount of the defect oxygen species on the surface, including chemisorbed oxygen species on oxygen vacancies (O_β) and hydroxyl-like groups such as chemisorbed

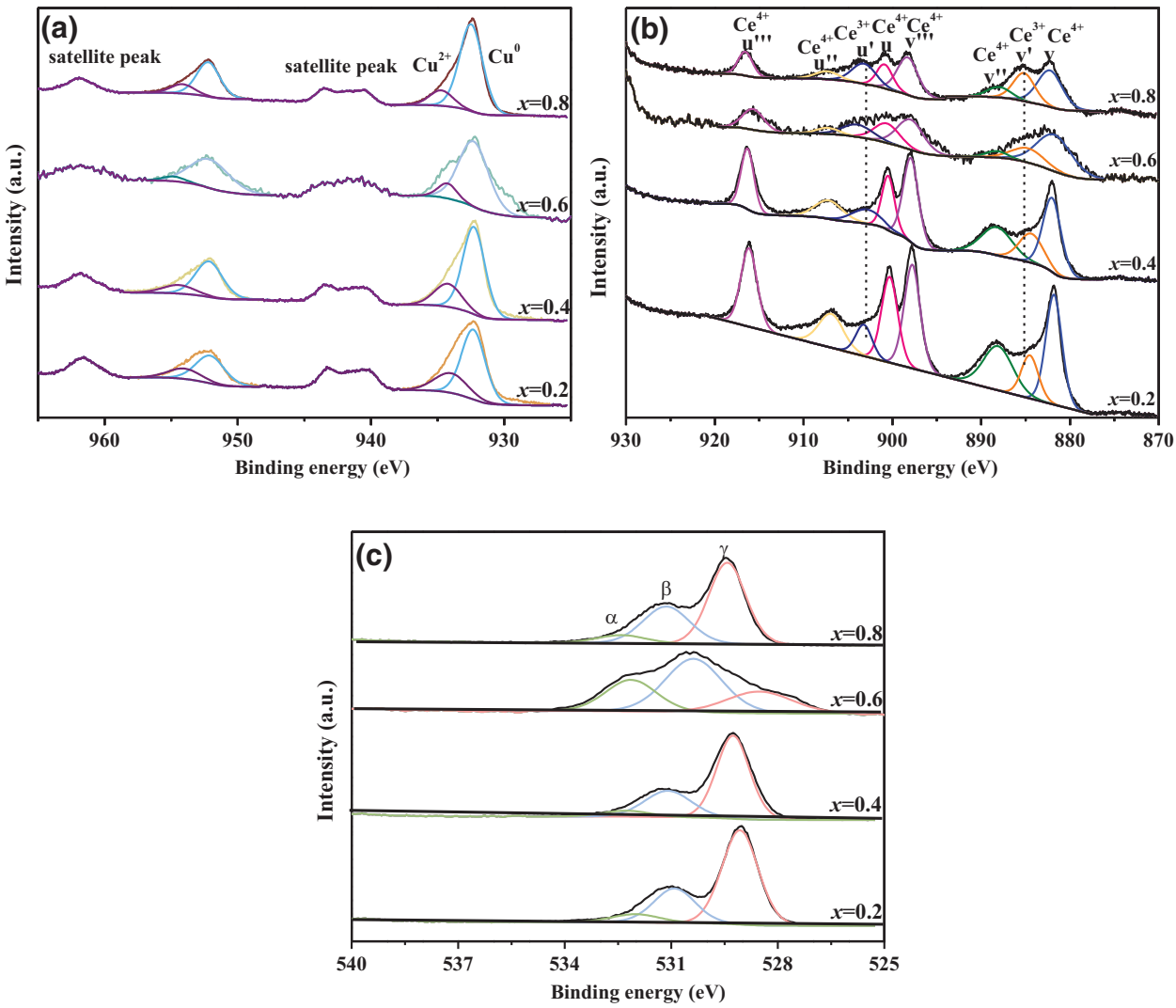

Fig. 4. XPS spectra of Cu 2*p* (a), Ce 3*d* (b) and O 1*s* (c) over H_2-reduced $CuO/Ce_{1-x}Zr_xO_2$ catalysts.

water (O_γ), vary with the amount of the ratio of Zr/Ce (Fig. 4c and Table 2). Importantly, $CuO/Ce_{0.4}Zr_{0.6}O_2$ catalyst shows the highest $O_\beta + O_\gamma$ concentration (49.1%), followed by $CuO/Ce_{0.2}Zr_{0.4}O_2$ (33.7%), $CuO/Ce_{0.6}Zr_{0.8}O_2$ (29.1%) and $CuO/Ce_{0.8}Zr_{0.2}O_2$ (27.2%). In summary, the number of Cu–Ce–Zr solid solution varies with the Zr/Ce ratio, and results in the different concentrations of oxygen vacancies, which will further facilitate the adsorption and activation of CO_2 on the surface and stabilize the reaction intermediates in the CO_2 hydrogenation to CH_3OH reaction [29]. Moreover, it is well known that the generation of oxygen vacancies will be beneficial for the formation of a strong metal-support interaction between Cu and $Ce_{1-x}Zr_xO_2$ [30]. Hence, the largest amount of oxygen vacancies over $x = 0.6$ leads to the stronger interaction between Cu and $Ce_{0.4}Zr_{0.6}O_2$.

3.4. Effect of Zr/Ce ratio on the adsorption behaviors of catalysts

The surface-adsorbed H_2 and CO_2 play key roles in CO_2 hydrogenation to CH_3OH, and Fig. 6 shows the H_2-TPD patterns of $CuO/Ce_{1-x}Zr_xO_2$ samples. Two H_2 desorption peaks are observed, a broad weak signal at 300–550 °C (Fig. 6a) and a strong signal at 550–750 °C (Fig. 6b). The former peak is assigned to the hydrogen species adsorbed on Cu in the form of Cu–H bonds [31]. The lower desorption temperature of former peak is observed over $CuO/Ce_{0.4}Zr_{0.6}O_2$ compared with other samples due to larger number of accessible Cu sites are conductive to the H_2 adsorption over $CuO/Ce_{0.4}Zr_{0.6}O_2$ sample [32]. The latter peak stems from the adsorbed spillover hydrogen from the Cu^0 species to the $Ce_{1-x}Zr_xO_2$ surface [33]. The intensity of latter peak is in the order of $x = 0.6 > x = 0.8 > x = 0.4 > x = 0.2$, indicating that $x = 0.6$ is much more favorable for the spillover of atomic hydrogen on the metal oxides.

Fig. 7 illustrates the CO_2 desorption curves over the H_2-reduced samples from 50 °C to 450 °C. The low-temperature region (<150 °C) is assigned to the weak basic sites; the 150–300 °C region is attributable to the middle basic sites while the high-temperature (>300 °C) region corresponds to the strong basic sites [34]. It is presented that, as shown in Fig. 7(a), $Ce_xZr_{1-x}O_2$ solid solution has amounts of weak basic sites while pure CuO mainly has the middle basic sites. In addition, as shown in Fig. 7(b), it is observed that the amount and intensity of each basic site on the Cu-containing catalysts is much higher than that on the Cu-free catalyst due to the interaction effect, especially for $CuO/Ce_{0.4}Zr_{0.6}O_2$ sample. The interaction between Cu and $Ce_{1-x}Zr_xO_2$ strongly improves the CO_2 adsorption capacity.

3.5. Catalytic performance of $CuO/Ce_{1-x}Zr_xO_2$

The H_2-reduced $CuO/Ce_{1-x}Zr_xO_2$ (x = 0.2, 0.4, 0.6, 0.8) catalysts are adopted to examine the catalytic performance for the CO_2

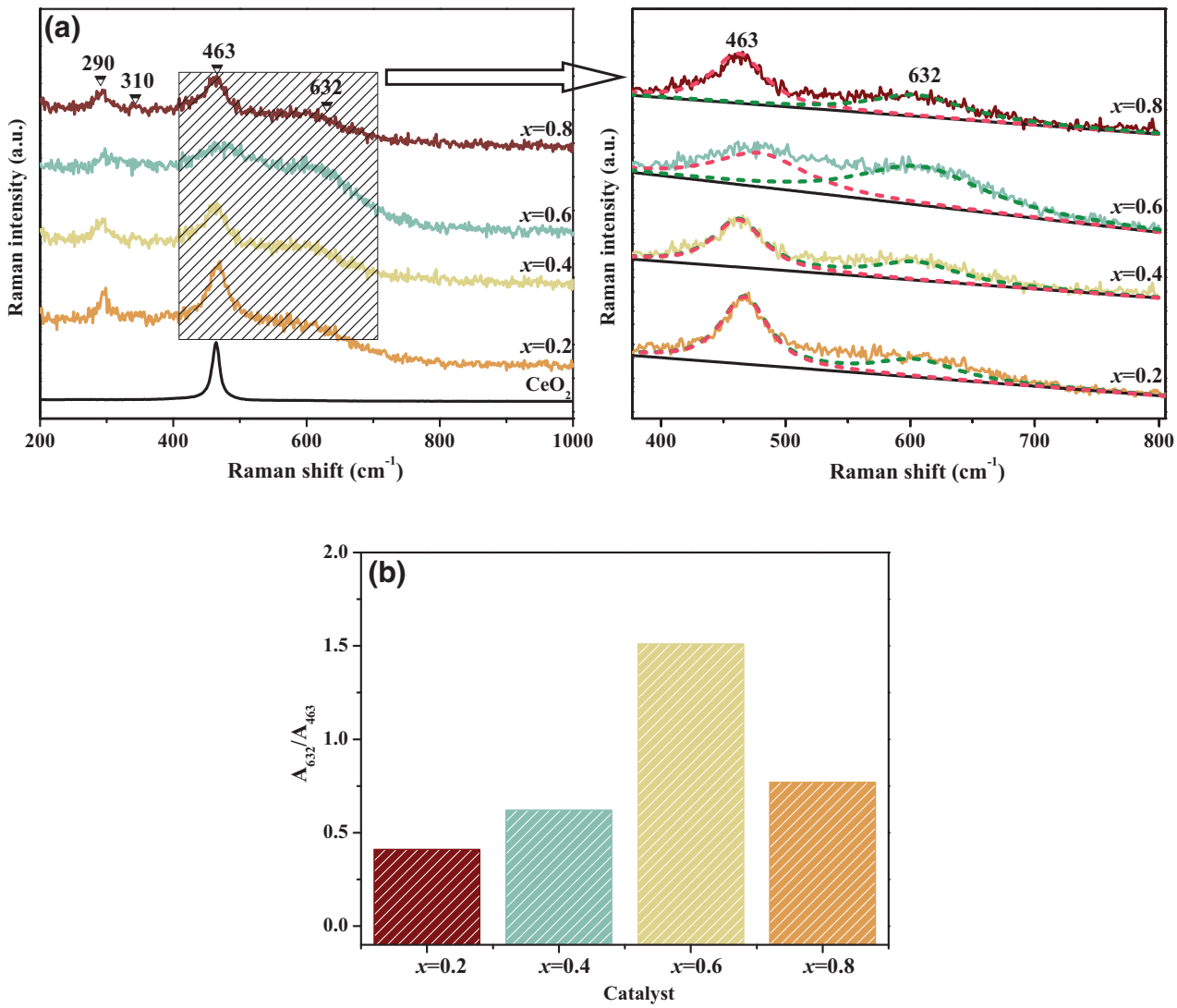

Fig. 5. Raman spectra of $CuO/Ce_{1-x}Zr_xO_2$ (a); and A_{632}/A_{463} of $CuO/Ce_{1-x}Zr_xO_2$ (b) catalysts.

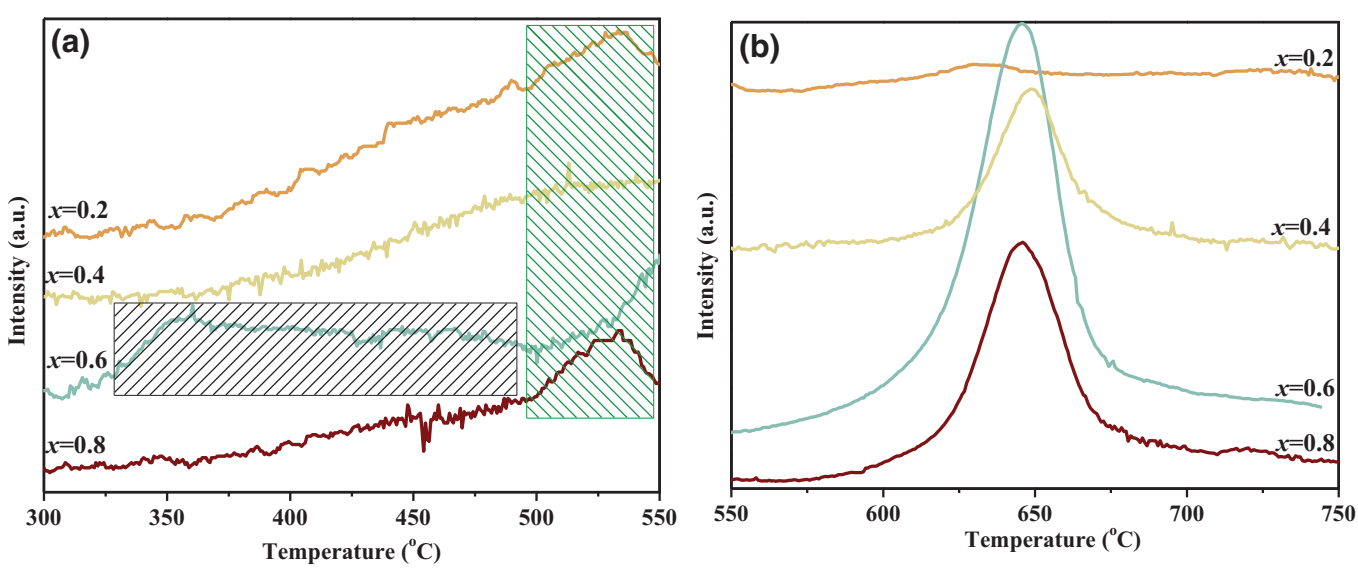

Fig. 6. H_2-TPD profiles of H_2-reduced $CuO/Ce_{1-x}Zr_xO_2$ catalysts from 300 to 550 °C (a) and from 550 to 750 °C (b).

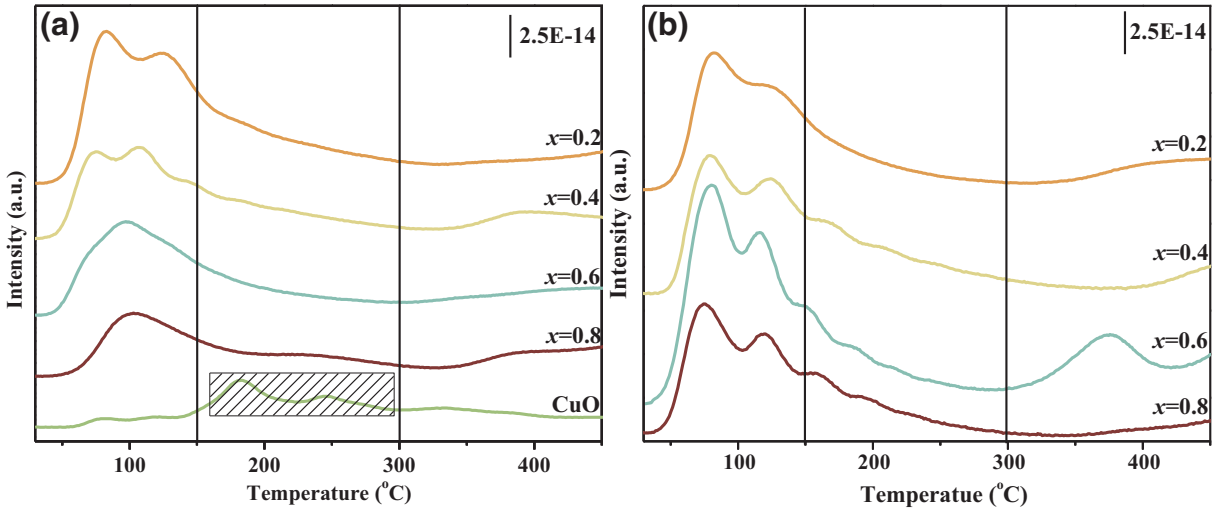

Fig. 7. CO_2-TPD profiles of $Ce_{1-x}Zr_xO_2$ (a) and $CuO/Ce_{1-x}Zr_xO_2$ (b) catalysts.

hydrogenation to CH_3OH. Fig. 8(a) illustrates the CO_2 conversion as a function of temperature over $CuO/Ce_{1-x}Zr_xO_2$ (x = 0.2, 0.4, 0.6, 0.8) catalysts. The CO_2 conversion is extremely low without the copper species and the value is below 3%. CO_2 conversion is enhanced greatly after adding CuO and the value differs by Zr/Ce ratio. Clearly, the activity of the H_2-reduced $CuO/Ce_{0.4}Zr_{0.6}O_2$ catalyst is better than that of the other catalysts from 200 to 300 °C. The CO_2 conversion of the $CuO/Ce_{0.4}Zr_{0.6}O_2$ catalyst is 5.4%, 7.0%, 9.2%, 9.9%, 13.2% and 15.6% at reaction temperature of at 200, 220, 240, 260, 280, 300 °C, respectively. Fig. 8(b) shows the CH_3OH selectivity of $CuO/Ce_{1-x}Zr_xO_2$ (x = 0.2, 0.4, 0.6, 0.8). The decrease in CH_3OH selectivity with increasing temperature has occurred mainly due to the shift of reaction towards RWGS reaction and CO_2 methanation [35]. The barely CH_3OH production is detected over $Ce_{0.4}Zr_{0.6}O_2$ solid solution. After the addition of copper into $Ce_{0.4}Zr_{0.6}O_2$ solid solution, the target CH_3OH selectivity increases in a great extent. The value of CH_3OH selectivity in the order is $x = 0.2 < x = 0.4 < x = 0.8 < x = 0.6$. The selectivity of the $CuO/Ce_{0.4}Zr_{0.6}O_2$ catalyst is about 97.8%, 96.4%, 93.9%, 85.7%, 71.8% and 40.6% at 200, 220, 240, 260, 280, 300 °C, respectively. What's more, the $x = 0.6$ sample also possesses the largest CH_3OH yield at all reaction temperatures, and the maximum value is 9.47% at 280 °C (Fig. 8c). The activity of the catalysts is also compared on the basis of turnover frequencies, which are calculated as molecules of CO_2 converted per second on Cu^0 surface site (TOF_{CO2} at 280 °C) (Fig. 8d). The $CuO/Ce_{0.4}Zr_{0.6}O_2$ sample shows the highest TOF_{CO2} value (0.13 s^{-1}). The comparison of catalytic properties between $CuO/Ce_{1-x}Zr_xO_2$ and benchmark Cu-ZnO-Al_2O_3 under the same conditions is presented in Fig. S1. A series of catalysts exhibit significantly different reaction performance, with the $CuO/Ce_{0.4}Zr_{0.6}O_2$ and $CuO/Ce_{0.2}Zr_{0.8}O_2$ catalyst having a higher CO_2 conversion (13.2% and 10.4%) than Cu-ZnO-Al_2O_3 (9.8%) and a dramatically higher CH_3OH selectivity (71.8% and 61.6%) than the latter (40.2%). To sum up, the $CuO/Ce_{0.4}Zr_{0.6}O_2$ sample present superior catalytic performance in terms of CO_2 conversion and CH_3OH production.

The role of Cu–CeO_2 and Cu–ZrO_2 interaction has been debated and previous our study suggest that the interaction has a positive influence on CH_3OH formation via CO_2 hydrogenation [9]. The ternary $CuO/Ce_{1-x}Zr_xO_2$ catalyst exhibits much higher methanol yield than either Cu/CeO_2 or Cu/ZrO_2, suggesting that the interaction should also play an important role in the $CuO/Ce_{1-x}Zr_xO_2$ catalyst for CO_2 hydrogenation. H_2-TPR (Fig. 3), N_2O chemisorption (Table 1) and H_2-TPD (Fig. 6) results prove that the CuO–$Ce_{1-x}Zr_xO_2$ interaction enhance the dissociation of H_2 and spillover of atomic hydrogen. As a result, more active H* species can participate in the CO_2 hydrogenation reaction, which are advantageous to inducing the hydrogenation of CO_2 to formate and methoxy, leading to the promotion of the activity of CO_2 hydrogenation to CH_3OH [36].Combining the results of XPS (Fig. 4) and CO_2-TPD (Fig. 7), it can be concluded that the CuO–$Ce_{1-x}Zr_xO_2$ interaction promotes the formation of oxygen vacancies, which should be the active sites for CO_2 adsorption. Then it is benefit to activate CO_2 and stabilize the reaction intermediates, elevating the catalytic performance [37]. The larger amount of oxygen vacancies and higher dispersion of Cu^0 species on the $CuO/Ce_{0.4}Zr_{0.6}O_2$ catalyst due to CuO–$Ce_{0.4}Zr_{0.6}O_2$ stronger interaction, which promotes the adsorption of CO_2, enhance the dissociation of H_2 and spillover of atomic hydrogen, bind the key reaction intermediates for further conversion, and increase the catalytic performance.

3.6. In situ DRIFTS study

The nature of intermediate species and the dynamics of CO_2 hydrogenation are studied using *in situ* DRIFTS. As shown in Fig. 9, it is shown that the monodenate/bidentate formate (m/bi-HCOO*) and terminal/ bridged methoxy (t/b-*OCH_3) are primary reaction intermediate species in the hydrogenation of CO_2 to CH_3OH over four tested samples. The employment of the reactive mixture (CO_2 + H_2) after 60 min results in the appearance of bi-HCOO* species at ν_s(OCO) = 1371, δ(CH) = 1405, ν_{as}(OCO) = 1583, δ(CH) + ν_s(OCO) = 2713 and ν(CH) = 2804 cm^{-1} as well as m-HCOO* species at 1295 and 1567 cm^{-1}. The bands centered at 1045 and 1471 cm^{-1} are assigned to t-*OCH_3 [38]. Meanwhile, the target product CH_3OH signals at 2832 and 2944 cm^{-1} are also detected. Differently, extra bands emerged at 1143 and 2921 cm^{-1} only appear on x = 0.6 and 0.8 samples, which are assigned to b-*OCH_3 species [39]. The unique bands at 1081 and 1340 cm^{-1} corresponding to b-*OCH_3 and m-HCOO* species, respectively, on x = 0.2 and 0.4 samples [38]. Notably, the surface coverage of each intermediate species is much larger over $CuO/Ce_{0.4}Zr_{0.6}O_2$ than other samples, laying foundation for the superior catalytic performance, which is due to the stronger adsorption of CO_2 and H_2 as is described above results.

Comparing with Fig. 10(a–d), the types of surface intermediate species of ceria-rich samples (x = 0.2 and 0.4) are similar to the one recorded over the zirconia-rich samples (x = 0.6 and 0.8). The formate pathway can be identified for the CO_2 hydrogena-

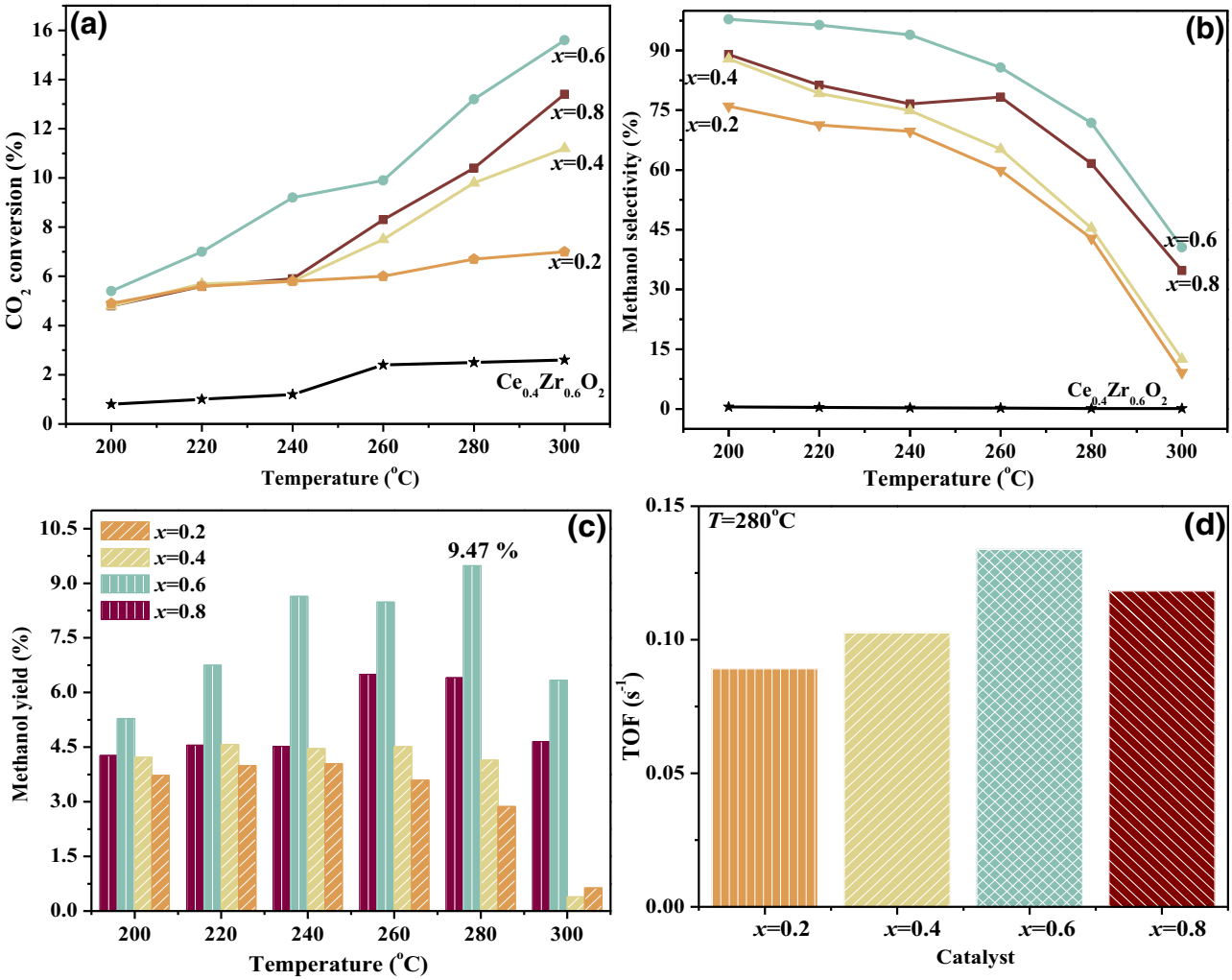

Fig. 8. CO_2 conversion (a), CH_3OH selectivity (b), CH_3OH yield (c) and TOF_{CO2} (d) of $CuO/Ce_{1-x}Zr_xO_2$ catalysts.

tion to CH_3OH process over the $CuO/Ce_{1-x}Zr_xO_2$ catalysts. However, the surface concentration and evolution of intermediate species are remarkably different. Seemingly, bi-HCOO* species keeps growing during the whole process on four samples. Another discovery is that the change trend of t-*OCH_3 exactly follows that of bi-HCOO* species (Fig. S2). At the initial stage (5 min), the higher surface coverage of bi-HCOO* and m-HCOO* species is observable on ceria-rich (x = 0.2 and 0.4) samples than those on zirconia-rich (x = 0.6 and 0.8) samples (Fig. S3). The above results demonstrate that ceria-rich samples are conducive to the accumulation

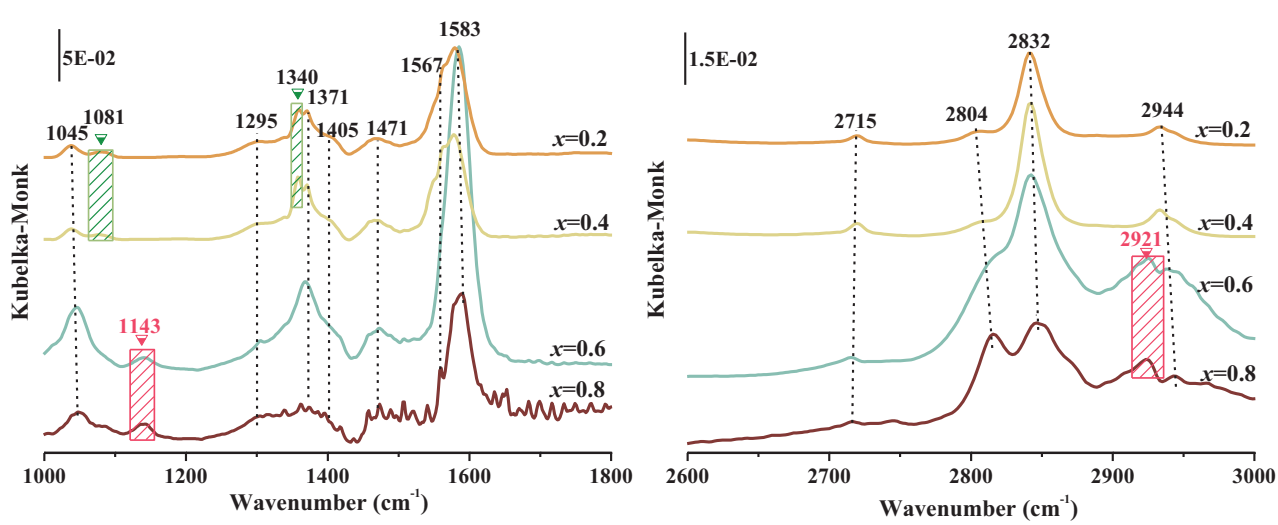

Fig. 9. *In situ* DRIFT spectra of CO_2 + H_2 on H_2-reduced $CuO/Ce_{1-x}Zr_xO_2$ catalyst at 1000–2000 cm^{-1} and 2600–3000 cm^{-1} at 60 min.

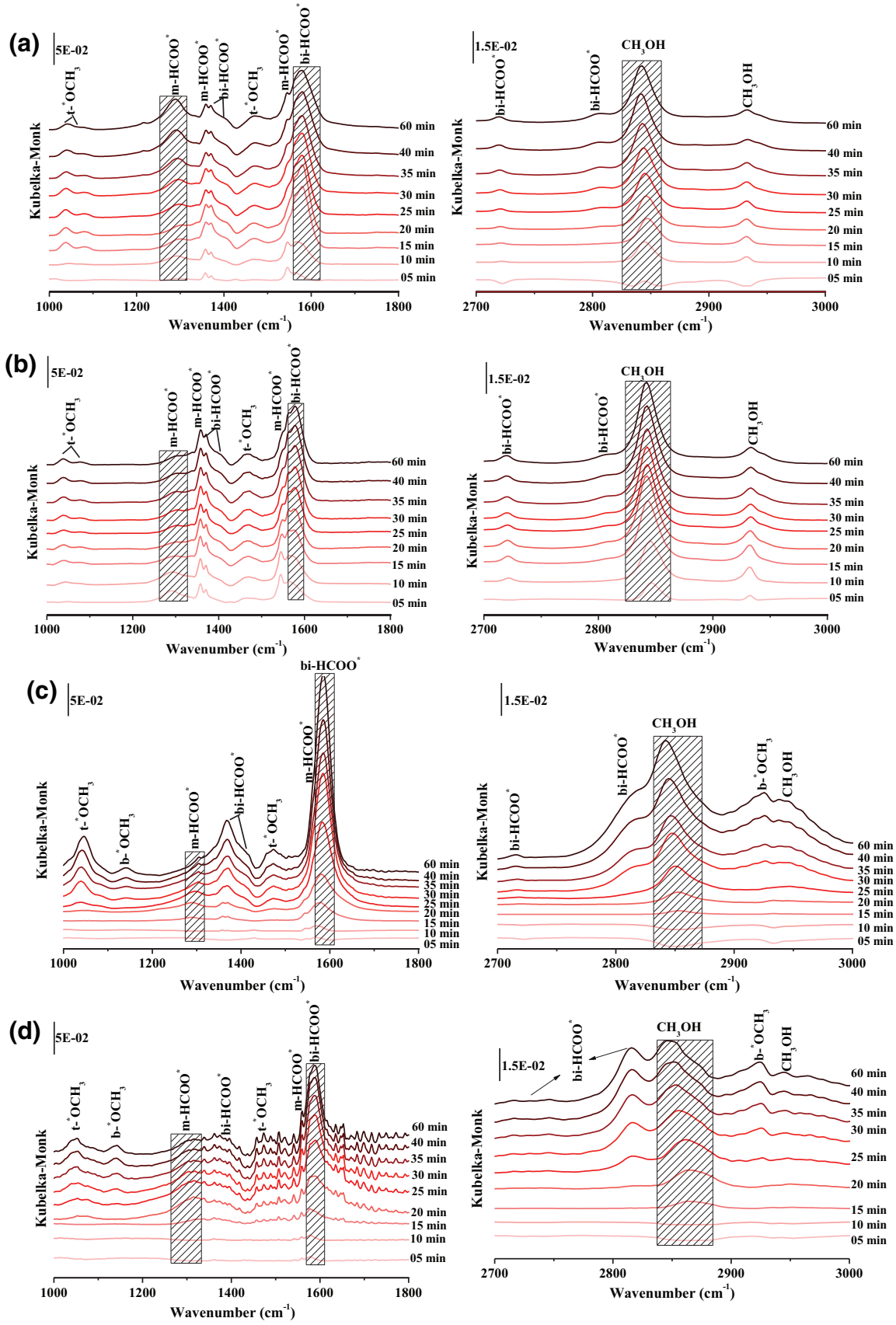

Fig. 10. The evolution of intermediate species with time on H_2-reduced (a) $CuO/Ce_{0.8}Zr_{0.2}O_2$ (x = 0.2); (b) $CuO/Ce_{0.6}Zr_{0.4}O_2$ (x = 0.4); (c) $CuO/Ce_{0.4}Zr_{0.6}O_2$ (x = 0.6); (d) $CuO/Ce_{0.2}Zr_{0.8}O_2$ (x = 0.8) catalysts.

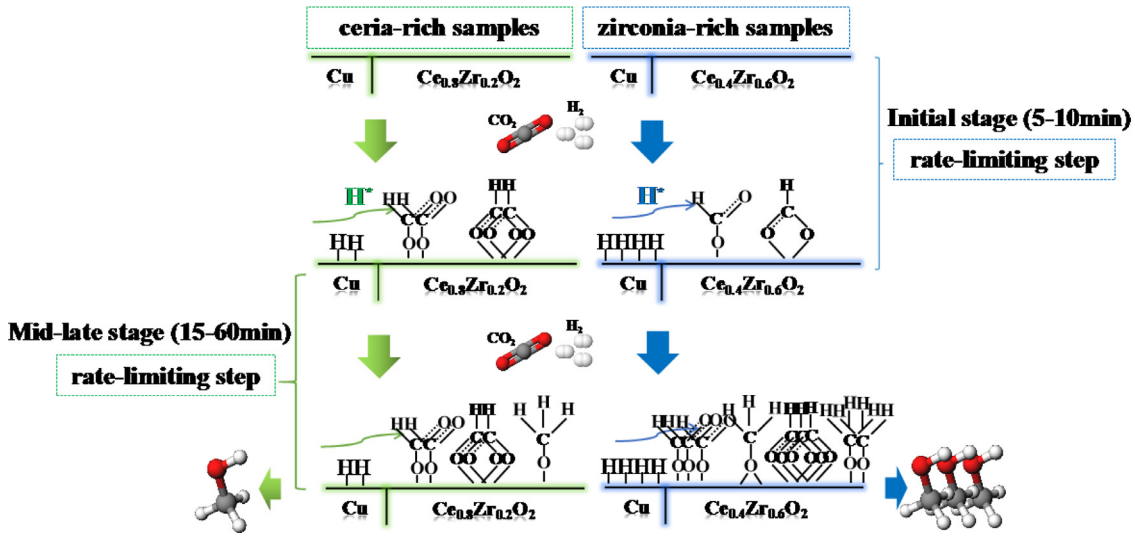

Scheme 1. The evolution of intermediate species on H_2-reduced $CuO/Ce_{0.8}Zr_{0.2}O_2$ ($x = 0.2$) and $CuO/Ce_{0.4}Zr_{0.6}O_2$ ($x = 0.6$) catalysts.

of formate (m/bi-HCOO*) species at the initial stage. Hence, at the starting stage, the higher concentration of CH_3OH is detected on ceria-rich samples (Fig. S3). However, the increase rate of bi-HCOO* is much higher on $x = 0.6$ sample, resulting in the formation of the highest concentration of bi-HCOO* on $x = 0.6$ sample after 30 min (Fig. 9), which is benefit to the production of CH_3OH [40]. Finally, $x = 0.6$ sample has the highest CH_3OH selectivity ($T = 280$ °C, S_{CH3OH} =71.8%).

The evolution of m-HCOO* is particularly different comparing with ceria-rich samples and zirconia-rich samples. The concentration of m-HCOO* species on $x = 0.2$ sample keeps going up while depletion of m-HCOO* at a slow rate is observed on $x = 0.4$ sample during the whole process. However, it is shown that the m-HCOO* species firstly go through a process of accumulation to 30 min and then consumption from 30 min to 60 min on $x = 0.6$ and $x = 0.8$ samples (Fig. S4). Hence, we make a conclusion that m-HCOO* species on zirconia-rich samples are much easier for further hydrogenation. Additionally, the concentration of m-HCOO* over $x = 0.6$ catalyst is more rapidly decreased compared to $x = 0.8$ sample, indicating that m-HCOO* species are more reactive on the $x = 0.6$ sample surface. This effect is attributed to the higher effectiveness of Cu to dissociate H_2 [41]. Almost concurrently with the consumption of m-HCOO* species, the bands owing to b-*OCH_3 and CH_3OH are observed to be greatly increased from 30 min (Fig. 10c and d). Hence, at last, the largest number of CH_3OH is detected on $x = 0.6$ sample.

The *in situ* DRIFTS experiments reveal that tuning the interaction between CuO and $Ce_{1-x}Zr_xO_2$ by modulating Zr/Ce ratio can affect the formation and evolution of formate species regarded as the most significant intermediate species of CO_2 hydrogenation to methanol [34]. The formation of CH_3OH arises from the hydrogenation of m-HCOO* and bi-HCOO*, suggesting that both m-HCOO* and bi-HCOO* are reactive intermediates. Differently, as shown in Scheme 1, the initial concentration of formate species on ceria-rich samples are higher but it is difficult to be further converted into methoxyl species, indicating that the hydrogenation of formate may be the rate-limiting step of CO_2 hydrogenation to methanol on ceria-rich samples. Differently, the formation of formate species on zirconia-rich samples takes a while but these are readily to be hydrogenated into methoxyl, and then to methanol, implying that the accumulating of formate species is probably the rate-limiting step of CO_2 hydrogenation to methanol on zirconia-rich samples. The above results indicate that Zr/Ce has obvious influence on the evolution of intermediate species as well as the rate-limiting step for the CO_2 hydrogenation to methanol, which will eventually affect the activity and selectivity of the catalyst.

4. Conclusions

The work explores the effects of Zr/Ce molar ratio on catalytic activity of $CuO/Ce_{1-x}Zr_xO_2$ samples. The strong interaction effect over $CuO/Ce_{0.4}Zr_{0.6}O_2$ catalyst contributes to the remarkable catalytic activity for CO_2 hydrogenation to CH_3OH, which leads to higher surface dispersion CuO and larger number of oxygen vacancies, promoting H_2 and CO_2 adsorption ability, thus giving rise to high catalytic performance (Y_{CH3OH} = 9.47%), compared with other catalysts. Additionally, *in situ* DRIFTS suggest that ceria-rich samples are much easier to enrich m-HCOO* and bi-HCOO* species while zirconia-rich samples are more benefit to promote the hydrogenation of m-HCOO* and bi-HCOO* species, besides the former ones are more active than the later ones. The decrease of larger number of active intermediate species m-HCOO* is responsible for the higher activity of CO_2 hydrogenation to CH_3OH over $CuO/Ce_{0.4}Zr_{0.6}O_2$ samples.

Declaration of Competing Interests

There are no conflicts to declare.

Acknowledgments

This work was financially supported by the National Nature Science Foundation of China (21876019, 21577014), Strategic Priority Research Program of the Chinese Academy of Sciences (XDB17020000), and the fund of the State Key Laboratory of Catalysis in DICP (N18-08).

Supplementary materials

Supplementary material associated with this article can be found, in the online version, at doi:10.1016/j.jechem.2019.11.021.

References

[1] I. Kima, G. Leea, H. Jeong, J.H. Park, J.C. Jung, J. Energy Chem. 26 (2017) 373–379.
[2] M. Bersani, K. Gupta, A.K. Mishra, R. Lanza, S.F.R. Taylor, H. Islam, N. Hollingsworth, C. Hardacre, N.H. de Leeuw, J.A. Darr, ACS Catal. 6 (2016) 5823–5833.

[3] H. Ahouari, A. Soualah, A. Le Valant, L. Pinard, P. Magnoux, Y. Pouilloux, React. Kinet. Mech. Cat. 110 (2013) 131–145.
[4] K. Samson, M. Śliwa, R.P. Socha, K. Góra-Marek, D. Mucha, D. Rutkowska-Zbik, J. Paul, M. Ruggiero-Mikołajczyk, R. Grabowski, J. Słoczyński, ACS Catal. 4 (2014) 3730–3741.
[5] M. Konsolakis, Appl. Catal. B 198 (2016) 49–66.
[6] H. Kim, J. Bae, S. Kang, K. Ha, K. Jun, W. Jang, K. Lee, B. Korean Chem. Soc. 31 (2010) 470–472.
[7] E.L. Fornero, A.L. Bonivardi, M.A. Baltanás, J. Catal. 330 (2015) 302–310.
[8] K. Chen, X. Duan, H. Fang, X. Liang, Y. Yuan, Catal. Sci. Technol. 8 (2018) 1062–1069.
[9] W. Wang, Z. Qu, L. Song, Q. Fu, J. Energy Chem. 40 (2020) 22–30.
[10] L. Lin, S. Yao, Z. Liu, F. Zhang, N. Li, D. Vovchok, A. Martínez-Arias, R. Castañeda, J. Lin, S.D. Senanayake, D. Su, D. Ma, J.A. Rodriguez, J. Phys. Chem. C 122 (2018) 12934–12943.
[11] F. Vindigni, M. Manzoli, T. Tabakova, V. Idakiev, F. Boccuzzi, A. Chiorino, Appl. Catal. B 125 (2012) 507–515.
[12] E. Aneggi, C. de Leitenburg, A. Trovarelli, Catal. Today 181 (2012) 108–115.
[13] X. Sun, C. Gong, G. Lv, F. Bin, C. Song, Mater. Res. Bull. 60 (2014) 341–347.
[14] M. Haneda, T. Kaneko, N. Kamiuchi, M. Ozawa, Catal. Sci. Technol. 5 (2015) 1792–1800.
[15] D. Jeong, W. Jang, H. Na, J. Shim, A. Jha, H. Roh, J. Ind. Eng. Chem. 27 (2015) 35–39.
[16] H. Ban, C. Li, K. Asami, K. Fujimoto, Catal. Commun. 54 (2014) 50–54.
[17] J. Ye, C. Liu, D. Mei, Q. Ge, ACS Catal. 3 (2013) 1296–1306.
[18] S. Ali, L. Chen, F. Yuan, R. Li, T. Zhang, S.U.H. Bakhtiar, X. Leng, X. Niu, Y. Zhu, Appl. Catal. B 210 (2017) 223–234.
[19] S. Jeon, H. Ham, Y. Suh, J.W. Bae, RSC Adv. 5 (2015) 54806–54815.
[20] W. Huang, J. Yang, C. Wang, B. Zou, X. Meng, Y. Wang, X. Cao, Z. Wang, Mater. Res. Bull. 47 (2012) 2349–2356.
[21] P. Gao, R. Xie, H. Wang, L. Zhong, L. Xia, Z. Zhang, W. Wei, Y. Sun, J. CO Util. 11 (2015) 41–48.
[22] C. Vandergrift, A. Wielers, B. Joghi, J. Vanbeijnum, M. Deboer, M. Versluijshelder, J.W. Geus, J. Catal. 131 (1991) 178–189.
[23] L.M. Acuña, R.O. Fuentes, M.C.A. Fantini, D.G. Lamas, J. Phys. Chem. C 118 (2014) 11445–11453.
[24] L. Liu, Q. Yu, J. Zhu, H. Wan, K. Sun, B. Liu, H. Zhu, F. Gao, L. Dong, Y. Chen, J. Colloid Interf. Sci. 349 (2010) 246–255.
[25] F. Bin, R. Kang, X. Wei, Q. Hao, B. Dou, P. Combust. Inst. 37 (2019) 5507–5515.
[26] R. Kang, X. Wei, F. Bin, Z. Wang, Q. Hao, B. Dou, Appl. Catal. A 565 (2018) 46–58.
[27] B. Zhao, Q. Wang, G. Li, R. Zhou, J. Alloy. Compd. 508 (2010) 500–506.
[28] Z. Wu, M. Li, J. Howe, H.M. Meyer, S.H. Overbury, Langmuir 26 (2010) 16595–16606.
[29] N. Rui, Z. Wang, K. Sun, J. Ye, Q. Ge, C. Liu, Appl. Catal. B 218 (2017) 488–497.
[30] M. Liu, Y. Yi, L. Wang, H. Guo, A. Bogaerts, Catalysts 9 (2019) 275.
[31] Y.F. Bao, C.L. Huang, L.M. Chen, Y.D. Zhang, L. Liang, J.J. Wen, M.L. Fu, J.L. Wu, D.Q. Ye, J. Energy Chem 27 (2018) 381–388.
[32] P. Gao, F. Li, H. Zhan, N. Zhao, F. Xiao, W. Wei, L. Zhong, H. Wang, Y. Sun, J. Catal. 298 (2013) 51–60.
[33] T. Takeguchi, S. Furukawa, M. Inoue, J. Catal. 202 (2001) 14–24.
[34] W. Li, G. Zhang, X. Jiang, Y. Liu, J. Zhu, F. Ding, Z. Liu, X. Guo, C. Song, ACS Catal. 9 (2019) 2739–2751.
[35] R.A. Dagle, J.L. Hu, S.B. Jones, W. Wilcox, J.G. Frye, J.F. White, J.Y. Jiang, Y. Wang, J. Energy Chem. 22 (2013) 368–374.
[36] X. Jiang, X. Nie, X. Wang, H. Wang, N. Koizumi, Y. Chen, X. Guo, C. Song, J. Catal. 369 (2019) 21–32.
[37] X. Liu, K. Zhou, L. Wang, B. Wang, Y. Li, J. Am. Chem. Soc. 131 (2009) 3140–3141.
[38] S. Collins, M. Baltanas, A. Bonivardi, J. Catal. 226 (2004) 410–421.
[39] K. Pokrovski, A. Bell, J. Catal. 241 (2006) 276–286.
[40] X. Wang, H. Shi, J. Szanyi, Nat. Commun. 8 (2017), doi:10.1038/s41467-017-00558-9.
[41] B. Hu, Y.Z. Yin, G.L. Liu, S.L. Chen, X.L. Hong, S.C.E. Tsang, J. Catal. 359 (2018) 17–26.